(Fig. 3C). Coimmunoprecipitation of LOV1 and TRX-h5 was not successful, possibly because of conditions required for solubilizing LOV1. Nonetheless, the cumulative data indicate that LOV1 and TRX-h5 interact in some manner at the plasma membrane, consistent with the idea that TRX-h5 is guarded by LOV1.

The guard model accounts for plants having immunity to a myriad of pathogens while possessing a limited number of *R* genes (*2*, *3*). *R* gene limitation is possible because effector targets are limited, and pathogens (however numerous) secrete functionally redundant virulence effectors. This implies that *R* genes across plant species evolve to guard common targets (*14*). We have observed victorin sensitivity in oats, *Arabidopsis*, barley, rice, *Brachypodium* (*15*), and bean (fig. S6). Because victorin binds diverse thioredoxins (fig. S1) and sensitivity is conditioned by a NB-LRR gene (*LOV1*) in *Arabidopsis*, inseparable from the *Pc2* resistance gene in oats, and mapped to a genomic region rich in NB-LRR genes in barley (*15*), the data suggest that victorin sensitivity is evoked by a common mechanism across these species: by victorin binding to a thioredoxin that is guarded by a NB-LRR protein. Given this and the important defense functions of TRXs (*6*), it is possible that multiple pathogens target thioredoxins to enhance virulence (i.e., redundant virulence effectors). Notably, *C. victoriae* does not cause disease in *Arabidopsis* in the absence of *LOV1* or in oats in the absence of *Vb* (*5*). This is important because it implies that victorin production did not evolve in *C. victoriae* to inhibit TRX-h5–conferred defense. Rather, *C. victoriae* uses victorin solely in its capacity as a defeated effector to exploit *R* gene–mediated defense for disease susceptibility. This suggests that other defeated effectors could confer virulence if expressed by the appropriate pathogen.

Susceptibility to three other necrotrophic pathogens has been associated with *R*-like genes (*16*, *17*). Given the numbers of *R* genes in plant genomes and defeated virulence effectors collectively deployed by biotrophic pathogens, this study underpins the importance of understanding the limits to necrotroph exploitation of effector-triggered immunity (resistance-mediated susceptibility), so that future deployment of resistance does not lead to the emergence of new disease.

References and Notes

1. J. M. Lorang, T. A. Sweat, T. J. Wolpert, *Proc. Natl. Acad. Sci. U.S.A.* **104**, 14861 (2007).
2. J. D. G. Jones, J. L. Dangl, *Nature* **444**, 323 (2006).
3. B. J. DeYoung, R. W. Innes, *Nat. Immunol.* **7**, 1243 (2006).
4. T. A. Sweat, J. M. Lorang, E. G. Bakker, T. J. Wolpert, *Mol. Plant Microbe Interact.* **21**, 7 (2008).
5. T. J. Wolpert, L. D. Dunkle, L. M. Ciuffetti, *Annu. Rev. Phytopathol.* **40**, 251 (2002).
6. Y. Tada *et al.*, *Science* **321**, 952 (2008).
7. H. Cao, S. A. Bowling, A. S. Gordon, X. Dong, *Plant Cell* **6**, 1583 (1994).
8. T. A. Sweat, T. J. Wolpert, *Plant Cell* **19**, 673 (2007).
9. C. Laloi, D. Mestres-Ortega, Y. Marco, Y. Meyer, J. P. Reichheld, *Plant Physiol.* **134**, 1006 (2004).
10. See supplementary materials on *Science* Online.
11. T. J. Wolpert, V. Macko, W. Acklin, D. Arigoni, *Plant Physiol.* **88**, 37 (1988).
12. C. C. Mundt, *Phytopathology* **99**, 1116 (2009).
13. A. Marmagne *et al.*, *Mol. Cell. Proteomics* **6**, 1980 (2007).
14. T. Wroblewski *et al.*, *Plant Physiol.* **150**, 1733 (2009).
15. J. Lorang, A. Cuesta-Marcos, P. M. Hayes, T. J. Wolpert, *Mol. Breed.* **26**, 545 (2010).
16. E. D. Nagy, J. L. Bennetzen, *Genome Res.* **18**, 1918 (2008).
17. J. D. Faris *et al.*, *Proc. Natl. Acad. Sci. U.S.A.* **107**, 13544 (2010).

Acknowledgments: We thank J. Chang and M. Behrenfeld for valuable discussion. This work was supported in part by the Agriculture and Food Research Initiative Competitive Grants Program from the USDA National Institute of Food and Agriculture (grants 2005-35319-15361 and 2008-35319-18651) and by NSF grant IOS-0724954. OSU's mass spectrometry facility and core is in part supported by National Institute of Environmental Health Sciences grant P30ES200210.

Supplementary Materials

www.sciencemag.org/cgi/content/full/science.1226743/DC1
Materials and Methods
Figs. S1 to S6
References (*18*–*27*)

29 June 2012; accepted 5 September 2012
Published online 18 October 2012;
10.1126/science.1226743

Tug-of-War in Motor Protein Ensembles Revealed with a Programmable DNA Origami Scaffold

N. D. Derr,[1,2,3]* B. S. Goodman,[1]* R. Jungmann,[4,5] A. E. Leschziner,[6] W. M. Shih,[2,3,5] S. L. Reck-Peterson[1]†

Cytoplasmic dynein and kinesin-1 are microtubule-based motors with opposite polarity that transport a wide variety of cargo in eukaryotic cells. Many cellular cargos demonstrate bidirectional movement due to the presence of ensembles of dynein and kinesin, but are ultimately sorted with spatial and temporal precision. To investigate the mechanisms that coordinate motor ensemble behavior, we built a programmable synthetic cargo using three-dimensional DNA origami to which varying numbers of DNA oligonucleotide-linked motors could be attached, allowing for control of motor type, number, spacing, and orientation in vitro. In ensembles of one to seven identical-polarity motors, motor number had minimal affect on directional velocity, whereas ensembles of opposite-polarity motors engaged in a tug-of-war resolvable by disengaging one motor species.

Cytoplasmic dynein and kinesin-1 (referred to as "dynein" and "kinesin" here) are opposite-polarity, microtubule-based motors that are responsible for producing and maintaining subcellular organization via the transport of many cargos in eukaryotic cells (*1*, *2*). Defects in these transport processes have been linked to neurological diseases (*1*, *3*, *4*). Microtubules contain inherent structural polarity, polymerizing rapidly at their "plus" ends and more slowly at their "minus" ends (*5*), with dynein and kinesin driving most minus- and plus-end–directed microtubule transport, respectively (*2*). Although some transport tasks require a single motor type, many cargos use both dynein and kinesin and move bidirectionally on microtubules (*1*, *6*, *7*). The mechanisms that allow ensembles of identical-polarity motors to coordinate their activity and ensembles of opposite-polarity motors to achieve both processive movement and rapid switches in direction are unknown.

To dissect the biophysical mechanisms of motor-driven cargo transport, we designed a programmable, synthetic cargo using three-dimensional DNA origami (*8*, *9*) (also see supplementary materials and methods). The cargo consisted of a 12-helix bundle with 6 inner and 6 outer helices (Fig. 1A and fig. S1) (*10*). We refer to this structure as a "chassis," akin to an automobile chassis that serves as a skeletal frame for the attachment of additional components. The origami chassis was made by rapidly heating and slowly cooling an 8064-nucleotide, single-strand DNA (ssDNA) "scaffold" in the presence of 273 short, ssDNA "staples" (fig. S1A and tables S1 to S3), which hybridize with discontinuous regions of the scaffold to fold it into a desired shape. Selective inclusion of staples with extra "handle" sequences that project out from the chassis provide site- and sequence-specific attachment points for motors, fluorophores, or other chemical moieties (Fig. 1B).

[1]Department of Cell Biology, Harvard Medical School, Boston, MA 02115, USA. [2]Dana-Farber Cancer Institute, Boston, MA 02115, USA. [3]Department of Biological Chemistry and Molecular Pharmacology, Harvard Medical School, Boston, MA 02115, USA. [4]Department of Systems Biology, Harvard Medical School, Boston, MA 02115, USA. [5]Wyss Institute for Biologically Inspired Engineering, Harvard University, Boston, MA 02115, USA. [6]Department of Molecular and Cellular Biology, Harvard University, Cambridge, MA 02138, USA.

*These authors contributed equally to this work.
†To whom correspondence should be addressed. E-mail: reck-peterson@hms.harvard.edu

Next, we purified well-characterized model dynein and kinesin motors and covalently linked them to DNA oligonucleotide "antihandles" complementary to the handle sequences on the chassis. We used a minimal dimeric *Saccharomyces cerevisiae* dynein (*11*, *12*) and a minimal dimeric human kinesin-1 (*13*), both of which contained a $SNAP_f$-tag at their cargo-binding domain for oligonucleotide antihandle attachment.

We next assessed motor-chassis complex assembly. Gel-shift assays of the dynein chassis indicated an ~80% probability for individual dynein occupancy at each motor site on the chassis (Fig. 1C and fig. S2A). Due to kinesin's small size relative to dynein, similar assays with the kinesin chassis did not allow individual occupancy numbers to be resolved (fig. S2B). When the kinesin antihandle was used with dynein, however, we again observed ~80% occupancy, indicating no handle-sequence–specific effects on motor-chassis linking (fig. S2, C and D). Super-resolution fluorescence imaging with the use of DNA-PAINT (*14*) revealed that submaximal handle incorporation into the folded chassis was probably responsible for incomplete motor occupancy (fig. S3), in agreement with previous reports (*15*, *16*). Negative-stain transmission electron microscopy (TEM) of fully assembled chassis structures showed dynein motors occupying sites on the chassis at the programmed locations (Fig. 1D).

We quantified the motile properties of dynein alone or dynein ensembles on the chassis with one, two, four, or seven motor-attachment sites (1D, 2D, 4D, and 7D, respectively) on microtubules at the single-molecule level using total internal reflection fluorescence microscopy (Fig. 2A). The average velocity of a single dynein was similar to that of the 1D and 2D ensembles, whereas 4D and 7D ensembles moved slightly slower (Fig. 2B and fig. S4A). The characteristic run length (total distance moved) and time (total duration of the run) of the dynein ensembles increased with the number of motor sites for the 1D, 2D, and 4D ensembles (Fig. 2, C and D, and fig. S4, B and C). The 4D and 7D ensembles were

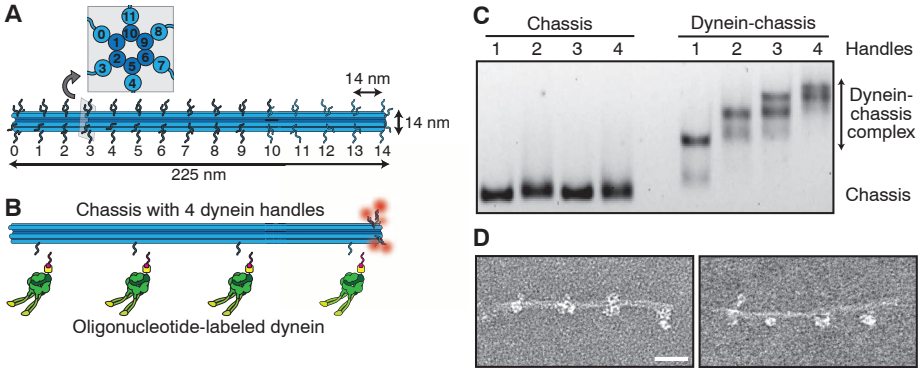

Fig. 1. Design and validation of a three-dimensional DNA origami synthetic cargo. (**A**) Schematic of the 12-helix-bundle chassis structure with 6 inner and 6 outer helices. Each outer helix contains up to 15 optional handles, yielding 90 uniquely addressable sites. Each handle consists of an unpaired 21-bp (~7 nm) oligonucleotide sequence for hybridization to complementary antihandle sequences covalently attached to motors or fluorophores. The inset shows an orthogonal cross section. (**B**) Schematic of a chassis labeled with five fluorophores (red) at handle position 14 on each of five outer helices and dynein handles at positions 1, 5, 9, and 13 on a single outer helix. Oligonucleotide-labeled dynein is also shown. (**C**) Agarose gel-shift assay of a carboxytetramethylrhodamine (TAMRA)–labeled chassis containing one to four handles in the absence (left lanes) or presence (right lanes) of dynein labeled with an antihandle oligonucleotide. Chassis are visualized by TAMRA fluorescence. See fig. S2B for occupancy quantification. (**D**) Negative-stain TEM images of the four-dynein–chassis complex. Scale bar, 40 nm.

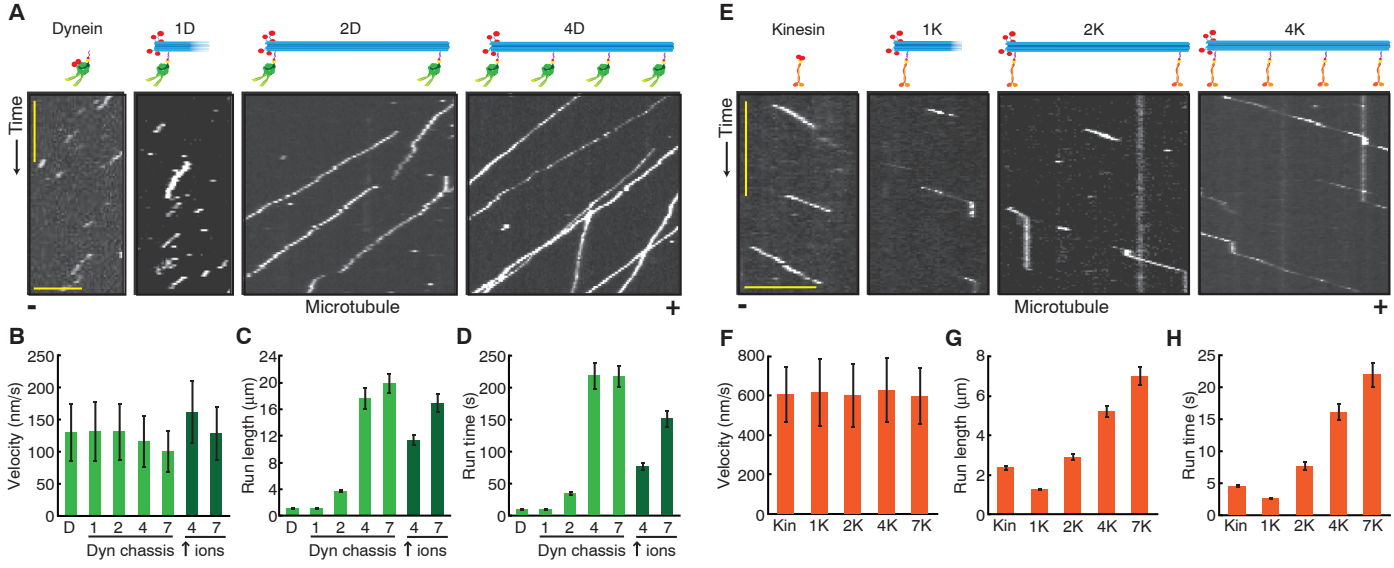

Fig. 2. Single-molecule motile properties of chassis-motor complexes. (**A**) Kymographs of a tetramethylrhodamine (TMR)–labeled dynein alone and a TAMRA-labeled chassis with 1, 2, or 4 dyneins. Plus (+) and minus (-) denote microtubule polarity. Scale bars: 1 min (*x* axis), 5 μm (*y* axis). (**B**) Quantification of average segment velocities ± SD (error bars) of dynein and dynein-chassis complexes. The 4D and 7D ensembles moved significantly slower than dynein alone or the 1D or 2D ensembles (one-tailed *t* test, $P < 0.001$; $N \geq 211$ runs). In higher ionic concentration (↑ ions), the 4D and 7D ensemble velocities were significantly different (one-tailed *t* test, $P < 0.001$; $N \geq 208$). (**C**) Quantification of run lengths ± SE (error bars) of dynein and dynein-chassis ensembles ($N \geq 208$). (**D**) Quantification of total run times ± SE (error bars) of dynein and dynein-chassis ensembles ($N \geq 208$). (**E**) Kymographs of TMR-labeled kinesin alone and a TAMRA-labeled chassis with 1, 2, or 4 kinesins. Scale bars: 1 min (*x* axis), 5 μm (*y* axis). (**F**) Quantification of average segment velocities ± SD (error bars) of kinesin and kinesin-chassis ensembles. Comparison of velocities yielded no statistical differences (analysis of variance test, $P > 0.05$; $N \geq 301$). (**G**) Quantification of run lengths ± SE (error bars) of kinesin and kinesin-chassis ensembles ($N \geq 301$). (**H**) Quantification of total run times ± SE (error bars) of kinesin and kinesin-chassis ensembles ($N \geq 301$). For additional statistical analysis, see figs. S4 to S6.

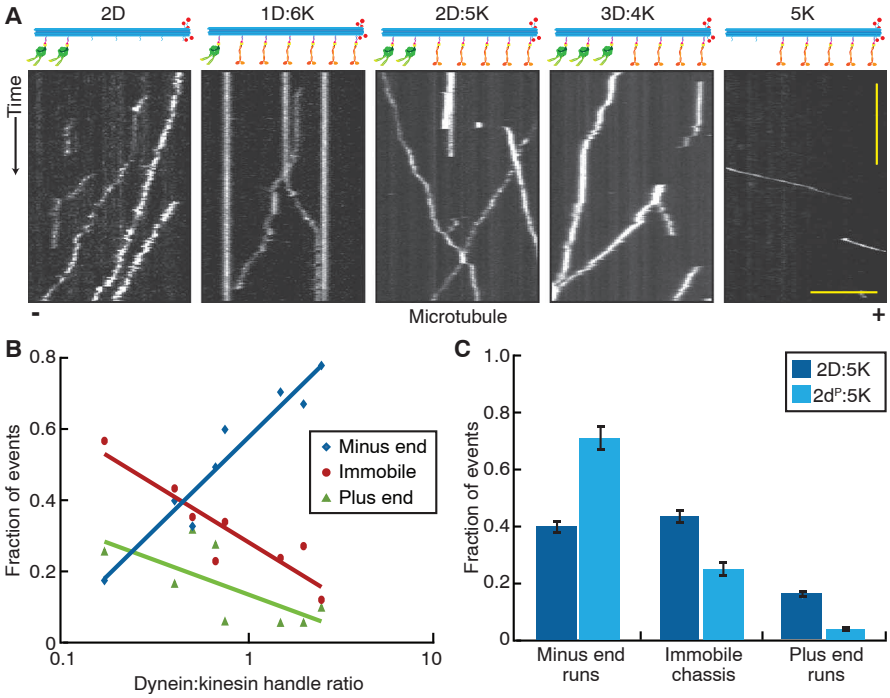

Fig. 3. Chassis attached to dynein and kinesin frequently engage in a stalled tug-of-war. (**A**) Kymographs of a TAMRA-labeled chassis attached to dynein only (leftmost panel), kinesin only (rightmost panel), or varying ratios of dynein and kinesin motors (middle panels). Plus (+) and minus (-) denote microtubule polarity. Scale bars: 1 min (*x* axis), 5 μm (*y* axis). (**B**) Quantification of the fraction of events for each chassis observed as defined by their dynein–to–kinesin-handle ratio. Chassis were immobile, moving toward the minus end, or moving toward the plus end ($N \geq 221$) (table S6). The *x* axis of dynein-to-kinesin ratios is a logarithmic scale, and linear-log fits highlight the trends observed. (**C**) Quantification of the fraction of events ± SE (error bars) observed to be immobile, moving toward the minus end, or moving toward the plus end for mixed ensembles containing two dyneins and five kinesins ($N \geq 352$). The dyneins were either wild type (D) or a highly processive mutant (d^P).

so processive that their run lengths and times were similar to each other in standard assay buffer, where microtubule length and imaging duration become limiting (Fig. 2, C and D). However, when assayed in high–ionic strength buffer, which decreases dynein's processivity (*17*), the 7D ensemble was more processive than the 4D ensemble (Fig. 2, C and D, and figs. S4 and S5).

We performed a similar analysis of kinesin alone and kinesin ensembles on the chassis with one, two, four, or seven motor-attachment sites (1K, 2K, 4K, and 7K, respectively; Fig. 2, E to H). The average velocities of the kinesin ensembles remained constant (Fig. 2F and fig. S6A), whereas run lengths and times increased with increasing motor number (Fig. 2, G and H, and fig. S6, B and C).

Recent models of motor ensemble behavior using a transition-state framework predict run lengths that are several orders of magnitude higher than what we observed (*18*). In contrast, our data suggest that motor microtubule binding dynamics may be influenced by the presence and number of other motors on a shared cargo, similar to previous work (*19*–*22*). For one to seven kinesins or one or two dyneins, velocity was unaffected by motor number. However, for 4D and 7D ensembles, velocity was decreased, suggesting that intermotor interference can affect motor stepping rate. To test this hypothesis, we engineered the chassis with locations for inactive mutant dyneins (denoted d^I) incapable of binding adenosine triphosphate (ATP) at dynein's main site of ATP hydrolysis; this mutant binds microtubules tightly, but does not move (*23*). Dynein ensembles programmed

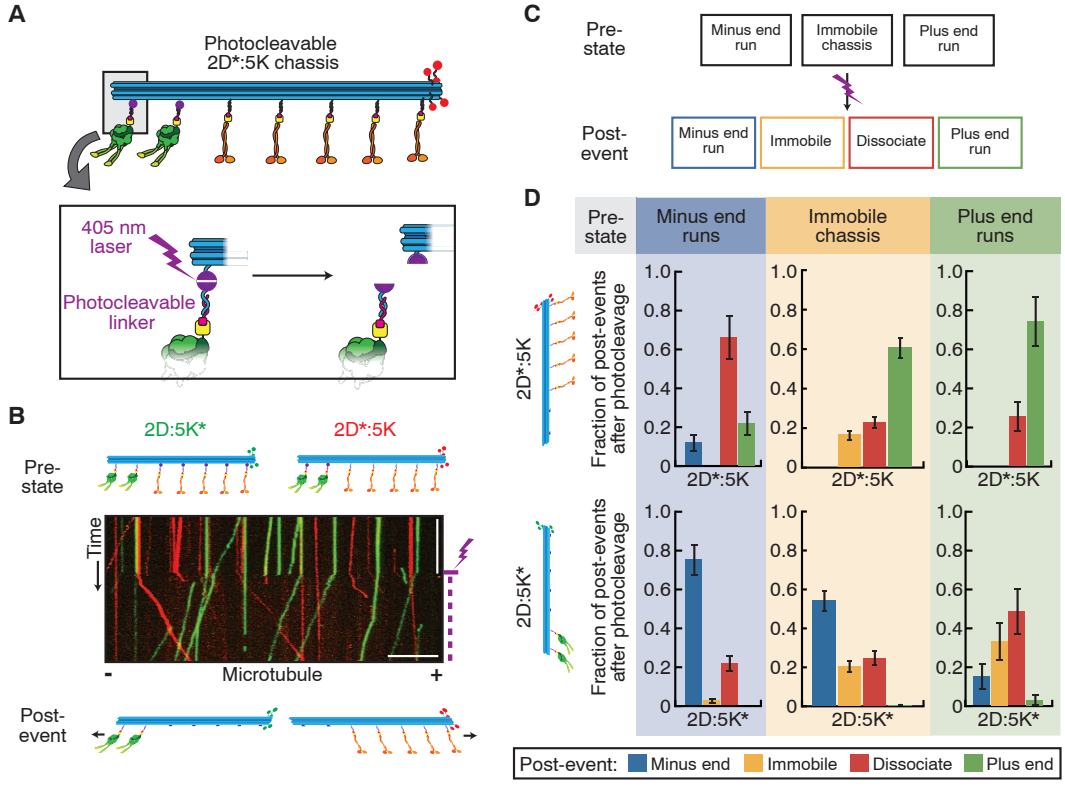

Fig. 4. Disengagement of one motor species resolves the stalled tug-of-war. (**A**) Schematic of a mixed-motor chassis with dynein attached via photocleavable handles (purple circles). Photocleavage is induced by 405-nm laser pulses (inset). (**B**) Kymograph of the 2D:5K*(green) and the 2D*:5K (red) chassis. The purple lightning bolt indicates the start of laser pulses. Plus (+) and minus (-) denote microtubule polarity. Scale bars: 1 min (*x* axis), 10 μm (*y* axis). (**C**) Chassis classification scheme for data presented in (D). Before (prestate) and after (postevent) laser photocleavage, the chassis were characterized as immobile, minus-end–directed, or plus-end–directed. Possible postevents also included dissociation from the microtubule. (**D**) Quantification of the postphotocleavage event motility of the 2D*:5K (top) and the 2D:5K* (bottom) chassis as a function of their prestates ($N \geq 286$). Each individual postevent fraction was calculated relative to the number of events within that given prestate. Error bars indicate SD.

to bind differing ratios of active and inactive motors (table S6) moved with reduced velocity (fig. S7), demonstrating that intermotor negative interference decreases cargo velocity.

We next investigated the motility of the chassis linked to mixed ensembles of opposite-polarity motors. We quantified the motility of the chassis as a function of the dynein-to-kinesin (D:K) ratio (table S6). All mixed-motor ensembles moved unidirectionally (Fig. 3A) with no reversals detected at a precision of ~10 nm. With the exception of the 1D:6K chassis, all ensembles were more likely to move toward the minus end of the microtubules (Fig. 3B). Mixed-motor ensembles were relatively insensitive to increasing the number of kinesin motors compared with increasing the number of dynein motors, which could be due to kinesin ensembles operating predominantly through the actions of fewer motors at any given time (*24*). Based on the stall forces of dynein [~5 pN (*25*)] and kinesin [~7 pN (*26*)], we expected that kinesin plus-end runs would have been more dominant. In contrast, our results suggest that stall force was not the only parameter governing the behavior of opposite-polarity motor ensembles (*27*). Other parameters, such as microtubule affinity, detachment force, and velocity-dependent on-rates, could also be relevant (*20*–*22*, *28*–*31*). Mixed-motor ensembles moved more slowly and for longer periods of time than did equivalent single-motor–type ensembles (fig. S8, A and B), with the magnitude of this effect being more pronounced in the plus-end direction. Notably, mixed ensembles of dynein and kinesin were more likely to be immobile than identical-motor ensembles, suggesting that opposite-polarity motors engage in a tug-of-war that prevents cargo movement (Fig. 3B).

Based on the longer run lengths and times of yeast dynein compared with human kinesin, we hypothesized that dynein runs dominated in mixed-motor ensembles due to dynein's higher microtubule affinity. To test this, we purified a mutant dynein with a higher processivity and affinity for microtubules (denoted d^P) (*17*) and paired it with kinesins. The $2d^P$:5K ensemble was even more likely to move in the dynein direction and had fewer immobile chassis structures compared with the 2D:5K ensemble containing wild-type (WT) dynein (Fig. 3C). These results suggest that track affinity is a key motor property in governing opposite-polarity motor ensemble motility. Mixed ensembles containing the high-affinity dynein mutant also produced slower plus-end runs and longer run times in both directions compared with the equivalent WT system (fig. S8, C and D).

We wanted to determine if mixed-motor ensembles were nonmotile due to a stalled tug-of-war. To regulate motor attachment to the chassis, we introduced photocleavable linkers in selected handles such that illumination with a 405-nm laser released one motor type from the chassis (Fig. 4A). We designed two modified chassis: (i) 2D:5K*, with photocleavable (*) kinesins, and (ii) 2D*:5K, with photocleavable dyneins. We monitored the motile properties of these chassis structures before and after laser-induced photocleavage (Fig. 4B). Cleavage was rapid (fig. S9); within seconds of photocleaving motors of one type, immobile chassis moved in the direction of the remaining motors (Fig. 4B). We classified the state of each chassis before and after photocleavage (Fig. 4C) and found that the majority of stalled tug-of-war events were resolved into active motility (Fig. 4D), indicating that disengagement of one motor type can resolve tug-of-war events between dynein and kinesin. Though we also observed rare events in which ensembles switched directions after photocleavage, we more commonly observed that chassis would dissociate when moving in the direction of the cleaved motor (fig. S10).

Using DNA origami, we built a versatile, synthetic cargo system that allowed us to determine the motile behavior of microtubule-based motor ensembles. In ensembles of identical-polarity motors, the motor number had a minimal affect on directional velocity, whereas ensembles of opposite-polarity motors engaged in a tug-of-war resolvable by disengaging one motor species. Yeast dynein's high microtubule affinity allowed it to dominate in mixed ensembles, whereas the ratio of dynein to kinesin dictated cargo directionality, supporting experiments performed in vivo or in cell-free lysates (*32*–*34*). The reduction in velocity reported here for opposite polarity motor ensembles also agrees with in vivo reports of dynein and kinesin tug-of-war (*32*, *35*). The high probability with which mixed ensembles of active dynein and kinesin motors were immobile suggested that, for this motor pair, efficient bidirectional transport requires extrinsic regulation (*36*). Motors with comparable microtubule affinities and binding kinetics, such as those that coevolved in the same biological system, may produce bidirectional transport characteristics similar to those observed in vivo (*6*, *37*, *38*). The system we built provides a powerful platform to investigate the motile properties of any combination of identical- or opposite-polarity motors and could also be used to investigate the role of motor regulation.

References and Notes

1. N. Hirokawa, S. Niwa, Y. Tanaka, *Neuron* **68**, 610 (2010).
2. R. D. Vale, *Cell* **112**, 467 (2003).
3. R. B. Vallee, J.-W. Tsai, *Genes Dev.* **20**, 1384 (2006).
4. G. T. Banks, E. M. C. Fisher, *Genome Biol.* **9**, 214 (2008).
5. A. Desai, T. J. Mitchison, *Annu. Rev. Cell Dev. Biol.* **13**, 83 (1997).
6. M. A. Welte, *Curr. Biol.* **14**, R525 (2004).
7. S. A. Bryantseva, O. N. Zhapparova, *Cell Biol. Int.* **36**, 1 (2012).
8. P. W. K. Rothemund, *Nature* **440**, 297 (2006).
9. S. M. Douglas *et al.*, *Nature* **459**, 414 (2009).
10. S. M. Douglas *et al.*, *Nucleic Acids Res.* **37**, 5001 (2009).
11. S. L. Reck-Peterson *et al.*, *Cell* **126**, 335 (2006).
12. W. Qiu *et al.*, *Nat. Struct. Mol. Biol.* **19**, 193 (2012).
13. R. B. Case, D. W. Pierce, N. Hom-Booher, C. L. Hart, R. D. Vale, *Cell* **90**, 959 (1997).
14. R. Jungmann *et al.*, *Nano Lett.* **10**, 4756 (2010).
15. Y. Ke, N. V. Voigt, K. V. Gothelf, W. M. Shih, *J. Am. Chem. Soc.* **134**, 1770 (2012).
16. S. H. Ko, G. M. Gallatin, J. A. Liddle, *Adv. Funct. Mater.* **22**, 1015 (2012).
17. W. B. Redwine *et al.*, *Science* **337**, 1532 (2012).
18. S. Klumpp, R. Lipowsky, *Proc. Natl. Acad. Sci. U.S.A.* **102**, 17284 (2005).
19. C. Leduc, N. Pavin, F. Jülicher, S. Diez, *Phys. Rev. Lett.* **105**, 128103 (2010).
20. A. R. Rogers, J. W. Driver, P. E. Constantinou, D. Kenneth Jamison, M. R. Diehl, *Phys. Chem. Chem. Phys.* **11**, 4882 (2009).
21. H. Lu *et al.*, *J. Biol. Chem.* **287**, 27753 (2012).
22. J. Xu, Z. Shu, S. J. King, S. P. Gross, *Traffic* **13**, 1198 (2012).
23. T. Kon, M. Nishiura, R. Ohkura, Y. Y. Toyoshima, K. Sutoh, *Biochemistry* **43**, 11266 (2004).
24. D. K. Jamison, J. W. Driver, A. R. Rogers, P. E. Constantinou, M. R. Diehl, *Biophys. J.* **99**, 2967 (2010).
25. A. Gennerich, A. P. Carter, S. L. Reck-Peterson, R. D. Vale, *Cell* **131**, 952 (2007).
26. A. Yildiz, M. Tomishige, A. Gennerich, R. D. Vale, *Cell* **134**, 1030 (2008).
27. P. E. Constantinou, M. R. Diehl, *J. Biomech.* **43**, 31 (2010).
28. M. Y. Ali *et al.*, *Proc. Natl. Acad. Sci. U.S.A.* **108**, E535 (2011).
29. R. D. Vale, F. Malik, D. Brown, *J. Cell Biol.* **119**, 1589 (1992).
30. A. Kunwar, M. Vershinin, J. Xu, S. P. Gross, *Curr. Biol.* **18**, 1173 (2008).
31. D. K. Jamison, J. W. Driver, M. R. Diehl, *J. Biol. Chem.* **287**, 3357 (2012).
32. V. Levi, A. S. Serpinskaya, E. Gratton, V. Gelfand, *Biophys. J.* **90**, 318 (2006).
33. M. Schuster, R. Lipowsky, M.-A. Assmann, P. Lenz, G. Steinberg, *Proc. Natl. Acad. Sci. U.S.A.* **108**, 3618 (2011).
34. M. Amrute-Nayak, S. L. Bullock, *Nat. Cell Biol.* **14**, 416 (2012).
35. V. Soppina, A. K. Rai, A. J. Ramaiya, P. Barak, R. Mallik, *Proc. Natl. Acad. Sci. U.S.A.* **106**, 19381 (2009).
36. A. Kunwar *et al.*, *Proc. Natl. Acad. Sci. U.S.A.* **108**, 18960 (2011).
37. S. E. Encalada, L. Szpankowski, C.-H. Xia, L. S. B. Goldstein, *Cell* **144**, 551 (2011).
38. M. J. Egan, K. Tan, S. L. Reck-Peterson, *J. Cell Biol.* **197**, 971 (2012).

Acknowledgments: We thank C. Lin for assistance with electron microscopy; F. Aguet for assistance with data analysis; J. Huang, W. Qiu, W.B. Redwine, and A. Roberts for helpful advice and critical reading of the manuscript; members of the Reck-Peterson and Shih labs for advice and helpful discussions; and J. Iwasa for illustrations. EM data were collected at the Center for Nanoscale Systems, Harvard University. DNA-PAINT data were collected at the Nikon Imaging Center, Harvard Medical School. R.J. is supported from the Alexander von Humboldt Foundation through a Feodor Lynen fellowship. S.L.R.-P. is funded by the Rita Allen Foundation, the Harvard Armenise Foundation, and a NIH New Innovator award (1 DP2 OD004268-1). W.M.S. is funded by NIH awards (1U54GM094608 and 1DP2OD004641) and ONR awards (N000014091118 and N000141010241).

Supplementary Materials

www.sciencemag.org/cgi/content/full/science.1226734/DC1
Materials and Methods
Figs. S1 to S10
Tables S1 to S6
Scaffold Sequence
References (*39*, *40*)
caDNAno File of Chassis Structure

29 June 2012; accepted 21 September 2012
Published online 11 October 2012;
10.1126/science.1226734